Objective delineation of lahar-inundation hazard zones

Richard M. Iverson* } *U.S. Geological Survey, Cascades Volcano Observatory, 5400 MacArthur Boulevard,*
Steven P. Schilling } *Vancouver, Washington 98661*

James W. Vallance *Department of Civil Engineering and Applied Mechanics, McGill University, Montreal, Quebec H3A 2K6, Canada*

ABSTRACT

A new method of delineating lahar hazard zones in valleys that head on volcano flanks provides a rapid, objective, reproducible alternative to traditional methods. The rationale for the method derives from scaling analyses of generic lahar paths and statistical analyses of 27 lahar paths documented at nine volcanoes. Together these analyses yield semiempirical equations that predict inundated valley cross-sectional areas *(A)* and planimetric areas *(B)* as functions of lahar volume *(V)*. The predictive equations ($A = 0.05V^{2/3}$ and $B = 200V^{2/3}$) provide all information necessary to calculate and plot inundation limits on topographic maps. By using a range of prospective lahar volumes to evaluate *A* and *B*, a range of inundation limits can be plotted for lahars of increasing volume and decreasing probability. Resulting hazard maps show graphically that lahar-inundation potentials are highest near volcanoes and along valley thalwegs, and diminish gradually as distances from volcanoes and elevations above valley floors increase. We automate hazard-zone delineation by embedding the predictive equations in a geographic information system (GIS) computer program that uses digital elevation models of topography. Lahar hazard zones computed for Mount Rainier, Washington, mimic those constructed on the basis of intensive field investigations. The computed hazard zones illustrate the potentially widespread impact of large lahars, which on average inundate planimetric areas 20 times larger than those inundated by rock avalanches of comparable volume.

INTRODUCTION

Lahars are debris flows that originate on volcanoes and surge toward adjacent lowlands, potentially jeopardizing people and property downstream. Delineation of lahar hazard zones traditionally entails review of historical records as well as field identification of inundation limits of prehistoric lahars in valleys that head on volcano flanks (e.g., Crandell and Mullineaux, 1967, 1975). Interpolation and extrapolation of inundation limits of past lahars provide the basis for predicting areas prone to inundation by future lahars. As tools for interpolation and extrapolation, investigators may use calibrated flow-routing models (e.g., Laenen and Hansen, 1988; Macedonio and Pareschi, 1992; Costa, 1997) as well as intuition and judgment. However, a need sometimes arises to assess hazards from future lahars at volcanoes where data provide little basis for interpo-

lation, extrapolation, or model calibration—because historic and geologic records of past lahars are sparse, or investigations to document past lahars have not been conducted (e.g., W. Scott et al., 1995).

Here, we describe development, implementation, and testing of an alternative method for delineating lahar-inundation hazard zones. The method is rapid, objective, and reproducible, and can be used where data, time, funding, or personnel are inadequate for application of traditional methods. The central tenets of our method are similar to those of traditional methods (e.g., K. Scott et al., 1995): (1) inundation by past lahars provides a basis for predicting inundation by future lahars; (2) distal lahar hazards are confined to valleys that head on volcano flanks; (3) lahar volume largely controls the extent of inundation downstream; (4) voluminous lahars occur less often than small lahars; and (5) no one can foretell the size of the next lahar to descend a given drainage. Both certainties and uncertainties implied in these tenets are reflected in our methodology.

Our method combines statistical analyses of lahar-inundation data from nine volcanoes with scaling analyses of lahar kinematics to develop semiempirical equations that predict the valley cross-sectional area (*A*) and planimetric area (*B*) inundated by lahars with various volumes (*V*). Scaling analyses described in the Physical Basis section of the paper provide the rationale for positing proportionality rules, $A \propto V^{2/3}$ and $B \propto V^{2/3}$, that relate *A*, *B*, and *V*. Data and statistics that test the validity of these rules and calibrate the values of proportionality coefficients are summarized in the Statistical Basis section. The calibrated predictive equations, $A = 0.05V^{2/3}$ and $B = 200V^{2/3}$, provide all information necessary to calculate and plot inundation limits on topographic maps.

Although it is possible to apply the predictive equations manually, using only a ruler to plot inundation limits on topographic maps, we automate the mapping process by embedding the predictive equations in a GIS (geographic information system) computer program that utilizes a digital elevation model (DEM) of topography. The Implementation section of the paper explains the GIS algorithm. The GIS allows us to delineate simultaneously the projected inundation areas for a variety of lahar volumes and to thereby depict gradations of the inundation hazard, which is greatest in valley thalwegs close to the volcano and diminishes as elevations above valley floors and distances from the volcano increase. Automated portrayal of gradations in hazard is one of the chief advantages of the GIS methodology.

The Results section of the paper presents examples of lahar hazard zones we have computed for Mount Rainier, Washington, and compares these zones with those generated using traditional methods. The Discussion section considers some ramifications of our findings for contrasting the inundation patterns of lahars, rock avalanches, and nonvolcanic debris flows as well as for probabilistic hazard assessments.
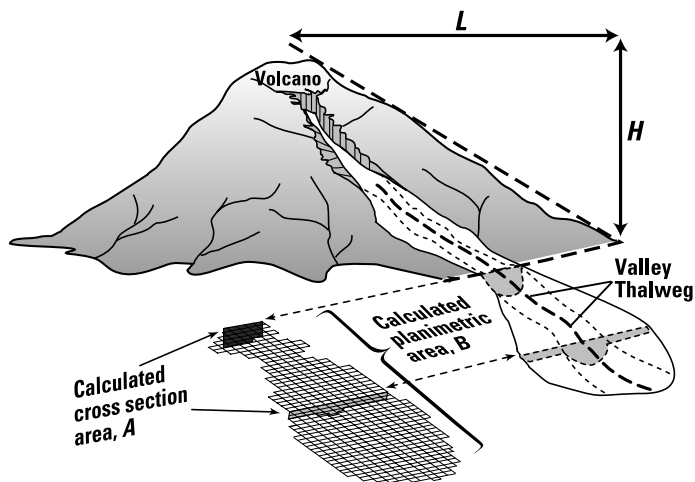
*E-mail: riverson@usgs.gov.

Figure 1. An idealized lahar path and geometric relationships between H and L, which describe the extent of the proximal hazard zone, and A and B, which describe the extent of the distal lahar-inundation hazard zone.
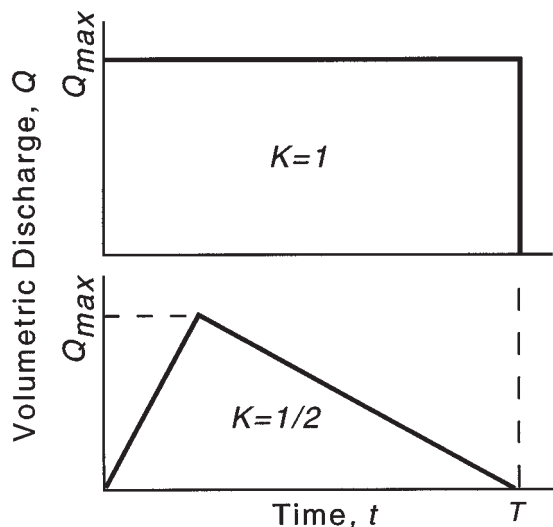

Figure 2. Idealized lahar hydrographs illustrating definitions of the lahar duration, T, and maximum instantaneous volumetric discharge Q_{max}, for hydrographs with different shape parameters, K.

PHYSICAL BASIS

Our method predicts inundation areas in distal valleys that head on volcano flanks, but distal lahars originate at proximal sources, and identification of source areas poses a preliminary problem. We narrow the scope of the problem by focusing on sudden-onset lahars that typically evolve from rock and ice avalanches, pyroclastic flows, or lake-breakout floods that originate high on volcano flanks or at the summit. These sudden-onset lahars are generally less predictable and more hazardous than lahars that develop gradually during rainfall runoff. We assume that source areas for sudden-onset lahars lie within a proximal hazard zone defined by the intersection of an "energy cone" with the volcano's topographic surface (cf. Malin and Sheridan, 1982). The energy cone has its apex at the volcano summit, and the cone slope is de-

termined by the characteristic ratio of vertical descent (H) to horizontal runout (L) of events such as pyroclastic flows or rock avalanches that may spawn lahars (Fig. 1). Values of H/L that define boundaries of proximal hazard zones commonly range from about 0.1 to 0.3, depending on the size and type of the proximal event (Hayashi and Self, 1992). Regardless of the choice of H/L values for defining proximal hazard zones, we assume that where the proximal hazard boundaries transect valleys, they define the upstream boundaries for delineating distal hazard zones. Lahar volume might vary in both the proximal and distal hazard zones, but operationally, we define the volume of a distal lahar as that which exits the proximal hazard zone.

In distal valleys lahar volume generally influences the size more than the shape of areas inundated. For example, viewed at a scale of 1:100 000, the paths of great lahars ($V \sim 10^9$ m³) can resemble those of commonplace lahars ($V \sim 10^6$ m³) viewed at a scale of 1:1000 (i.e., fractal scaling). If the shape of all lahar paths were identical, geometric similarity alone would establish the validity of the relationships $A \propto V^{2/3}$ and $B \propto V^{2/3}$. However, because the shape of lahar paths varies, it is useful to consider how the same relationships result from scaling analyses of lahar kinematics and geometries.

Analysis of Cross-Sectional Area Inundated (A)

To assess the cross-sectional area (and thereby the lateral limits) of valley inundation, consider a lahar that moves downstream as an evolving, translating waveform of constant mass and constant bulk density. For such a lahar conservation of mass implies conservation of volume, expressed by

$$V = \int_T Q(t)dt = KQ_{max}T. \qquad (1)$$

Here, V is total lahar volume, $Q(t)$ is the volumetric discharge at a valley cross section through which the lahar passes, Q_{max} is the maximum instantaneous (peak) volumetric discharge at the cross section, t is time, and T is the total time required for the lahar to pass the cross section. The shape of the lahar hydrograph determines the dimensionless parameter K (Fig. 2). The plausible range of K is $0 < K \leq 1$, but values of $K \sim 1/2$ are appropriate for most debris-flow hydrographs, which have shapes that are roughly triangular (Iverson, 1997). We assume that the maximum lahar discharge produces the maximum inundation of valley cross-sectional area, which is a quantity of primary interest for delineating hazard zones. Then Q_{max} and A_{max} are related by

$$Q_{max} = A_{max}U, \qquad (2)$$

in which U is the lahar velocity averaged over the valley cross section.

A key step in the scaling analysis involves recognition that U scales with the characteristic velocity $\sqrt{gR}$, in which g is the magnitude of gravitational acceleration and R is the hydraulic radius of the inundated valley cross section. (By definition, $R = A/P$, where A is the valley cross-sectional area inundated and P is the valley wetted perimeter [Fig. 3]). The scaling $U \sim \sqrt{gR}$ is fundamental for both unsteady and steady flows of liquids in open channels (e.g., Henderson, 1966). For example, $\sqrt{gR}$ is the approximate translation speed of ideal monoclinal waves in such flows, and the quantity $U^* = U/\sqrt{gR}$ is a dimensionless velocity commonly known as the Froude number, which characterizes the ratio of inertial and gravitational forces in such flows. A different (free-fall) velocity scaling may be more appropriate for rock avalanches and debris flows on steep slopes (Savage and Hutter, 1989; Iverson, 1997), but here we confine our attention to lahar behavior in distal regions, where valley thalwegs rarely slope more than 10°, and the scaling $U \sim \sqrt{gR}$ appears appropriate.

The velocity scaling $U \sim \sqrt{gR}$, combined with equation 2, produces the peak discharge scaling $Q_{max} \sim A_{max}\sqrt{gR}$ With this scaling we define the dimensionless peak discharge as

$$Q^*_{max} = \frac{Q_{max}}{A_{max}\sqrt{gR}}, \qquad (3)$$

in which the characteristic length scale $\sqrt{A_{max}}$ emerges as the counterpart to the characteristic velocity scale, $\sqrt{gR}$. In turn, the characteristic time scale results from the quotient of the characteristic length and velocity scales, $\sqrt{A_{max}}/\sqrt{gR}$. With this time scale we define the dimensionless lahar duration at a cross section as

$$T^* = \frac{T}{\sqrt{A_{max}}/\sqrt{gR}}. \qquad (4)$$

The desired relationship between A_{max} and lahar volume (V) results from using equations 3 and 4 in equation 1 and canceling redundant terms to obtain a dimensionless version of the mass-conservation equation,

$$V^* = V/A_{max}^{3/2} = KQ^*_{max}T^*. \qquad (5)$$

Adopting the simplified notation $C = (KQ^*_{max}T^*)^{-2/3}$, equation 5 may be expressed compactly as

$$A = CV^{2/3}, \qquad (6)$$

in which A is written as shorthand for A_{max}. If we assume that C is constant, which is equivalent to assuming that lahar hydrographs have constant shapes, then $A \propto V^{2/3}$.

Data summarized in the Statistical Basis section test the hypothesis that C is more or less constant and allow us to calibrate its value. With this calibration, equation 6 provides a means of calculating cross-sectional areas and lateral limits of lahar inundation in valleys with known cross-sectional shapes. Because equation 6 neglects downstream attenuation, it provides a conservatively large estimate of the maximum cross section inundated during lahar passage.

Analysis of Planimetric Area Inundated (B)

To assess the planimetric area and distal limit of downstream inundation, an additional equation is needed, because equation 6 implies that lahars travel downstream forever. Instead, as lahars move downstream they either lose momentum and come to rest—incrementally or abruptly—to form debris-flow deposits (Vallance and Scott, 1997), or they grow so dilute that sedimentation does not produce deposits that resemble those of debris flows (Pierson and Scott, 1985). For our purposes, we identify the distal extent of lahar deposits as the downstream limit of discernable overbank debris-flow deposition. Furthermore, because equation 6 constrains the lateral limits of inundation, we need only to determine the planimetric area of inundation to determine the distal limit of inundation (Fig. 1).

The relationship between lahar volume and planimetric area of inundation assumes that the lahar volume leaving the proximal hazard area (V) matches the volume deposited downstream. This is a simplistic assumption, because a lahar may gain or lose sediment and/or water and thereby alter its volume gradually as it moves downstream. However, most lahars grow in volume principally when crossing steep, proximal terrain (e.g., Pierson et al., 1990),
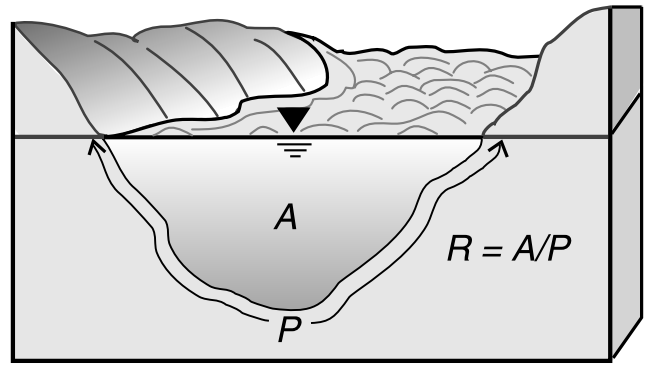

Figure 3. Definitions of the inundated hydraulic radius, R, inundated cross-sectional area, A, and wetted perimeter, P, of a valley occupied by a passing lahar.

and do not leave voluminous deposits until they begin to descend distal valleys (K. Scott et al., 1995). As a reasonable approximation (and a requisite for our analysis), we therefore regard distal lahar volume as a constant.

We assume the volume V of a distal lahar equals the volume of distal lahar deposits. Therefore,

$$V = \int_B h\,d\beta = \bar{h}B, \qquad (7)$$

in which β denotes infinitesimal planimetric elements of the distal lahar path, B denotes the total planimetric area of this path, and h denotes the lahar deposit thickness measured normal to the surface. The mean value of h in area B is $\bar{h}$, but equation 7 does not preclude the possibility of $h = 0$ (i.e., no deposition) in some parts of the distal lahar path.

Equation 7 can be simplified if $\bar{h} \propto B^{1/2}$ applies for lahar paths of diverse shapes and sizes. If all lahar paths were geometrically similar (i.e., had identical shapes and differed only in size), $\bar{h} \propto B^{1/2}$ would apply exactly. However, even if lahar paths differ significantly in planimetric shape, $\bar{h} \propto B^{1/2}$ applies approximately if $\bar{h}/\sqrt{B}$ is approximately constant (Fig. 4). Typically, $\bar{h}/\sqrt{B} \ll 1$ because lahar paths and deposits are dominantly tabular. Adopting the notation $\varepsilon = \bar{h}/\sqrt{B}$ and postulating that ε is a small constant, we substitute $\bar{h} = \varepsilon\sqrt{B}$ in equation 7 to rewrite the equation as $V = \varepsilon B^{3/2}$, or as

$$B = cV^{2/3}, \qquad (8)$$

in which $c = \varepsilon^{-2/3}$ is a hypothetical constant, $c \gg 1$. This equation expresses the desired relation between lahar volume and the planimetric area of inundation, but the validity of the equation and the constancy of c must be tested with data, as described in the next section.

STATISTICAL BASIS

To test and calibrate equations 6 and 8, we analyze trends in lahar-inundation data. Testing of the equations involves statistical determination of whether the inundation areas A and B are proportional to $V^{2/3}$, as equations 6 and 8 predict. Calibration of the equations entails statistical determination of the best-fit values of the proportionality coefficients c and C.

The power-law forms of equations 6 and 8 motivate us to linearize the equations by logarithmic transformation prior to statistical testing and calibration. Log transformation is appropriate because we expect the deviation
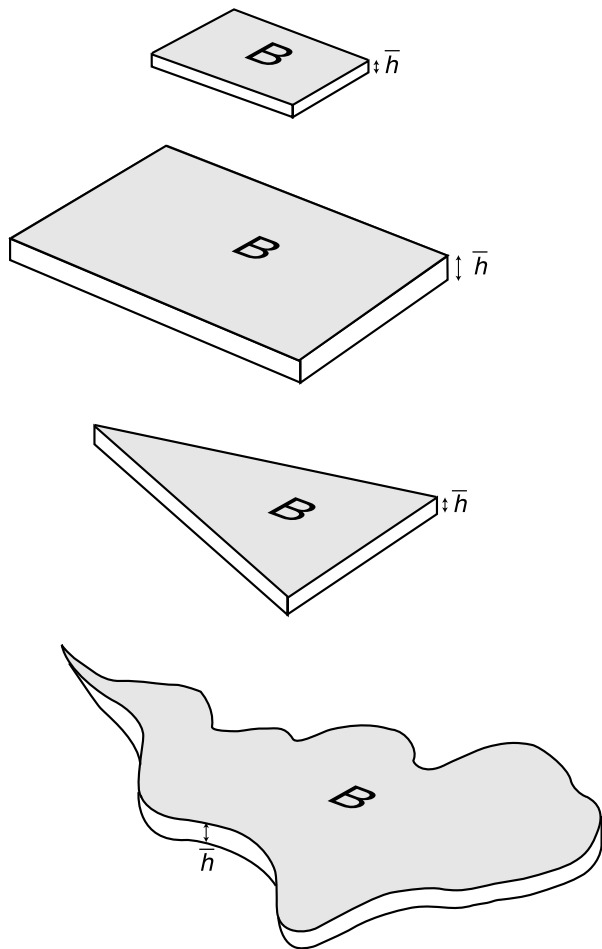
Figure 4. Idealized lahar-path geometries with $\bar{h}/\sqrt{B}$ constant.

of data values from a hypothetical trend to scale with the size of the data value. That is, we expect that the magnitude of the standard error of predictive equations will increase by a factor of 10 as lahar volume increases by a factor of 10. Log transformation of equation 6 yields

$$\log A = \log C + \frac{2}{3}\log V, \qquad (9)$$

in which 2/3 is the slope and $\log C$ is the A intercept (the value of $\log A$ where $\log V = 0$) on a log-log plot of A as a function of V. Similarly, log transformation of equation 8 yields

$$\log B = \log c + \frac{2}{3}\log V, \qquad (10)$$

in which 2/3 is the slope and $\log c$ is the intercept on a log-log plot of B versus V. In a statistical sense, equations 9 and 10 constitute null hypotheses; they provide a parsimonious model that can be rejected if data show that the actual relationship between $\log A$ (or $\log B$) and $\log V$ is nonlinear or has a slope significantly different from 2/3.

Data Attributes

Table 1 summarizes the data we use to test and calibrate equations 9 and 10 as well as data we use to compare lahars with smaller, nonvolcanic debris flows. The tabulated lahar volumes involve some uncertainty because lahars can vary in volume as they move downstream, and downstream changes in volume are not necessarily monotonic (e.g., Pierson, 1985, 1995; K. Scott et al., 1995). Furthermore, even lahars of constant volume needn't exhibit downstream attenuation of discharge or cross-section area. Therefore, the lahar volumes listed in Table 1 provide estimates of the single value most representative of the volume of any particular lahar as it enters the distal inundation area. (We do not use multiple volume estimates for individual lahars, even if they are available, because such data are not independent and would produce undesirable statistical bias.) In most cases the lahar volume we use is the estimated maximum instantaneous lahar volume, determined from deposited sediment volumes or from analyses of lahar hydrographs. Fortunately, even errors as large as 50% in volume estimation affect our results little, owing to our use of log-transformed data.

Additional uncertainty results from lack of historic data for large lahars. Our survey of the literature yielded no useful data for historic lahars with $V > 4 \times 10^7$ m^3. Nonetheless, lahars with $V > 10^9$ m^3 are evident in the geologic record, and prediction of inundation from such lahars can be crucial. Consequently, for lahars with $V > 4 \times 10^7$ m^3, we rely on data from 10 reconstructions of behavior of prehistoric lahars (Table 1). Although such data are commonly reported with considerable precision in the original references, we believe that the accuracy of such data is unlikely to exceed one significant digit. Our statistical analysis accommodates the probable lack of data accuracy for large events by using log-transformed data.

For lahars with volumes in the range 8×10^4 m^3 $\leq V \leq 4 \times 10^7$ m^3, we include data for 15 historic lahars that are generally documented better than are the larger prehistoric lahars (Table 1). Detailed documentation of historic lahars reveals complexities that may be camouflaged in the geologic record. For example, numerous discrete lahars were observed descending the Mabinit channel at Mayon volcano in the months following the eruption of 1984, yet these lahars formed a channel and deposit that would be difficult in retrospect to distinguish from that of a single lahar with several pulses or surges (Rodolfo, 1989). Data from experimental debris flows further demonstrate the difficulty of making such distinctions (Major, 1996). Consequently, for consistency with our statistical treatment of geologic reconstructions of prehistoric lahars, we treat the Mabinit lahars as though they constituted a single event.

Historic data also lead us to exclude from consideration a few well-documented lahars that were peculiar for obvious physical reasons. We exclude the North Fork Toutle River lahar that occurred on 18 May, 1980, at Mount St. Helens, Washington, because this lahar initiated exceptionally slowly by gradual leakage of sediment from a previously emplaced debris-avalanche deposit (Fairchild, 1987). We also exclude the Mount Ruapehu, New Zealand, lahars considered by Vignaux and Weir (1990), which were exceptionally dilute. Exclusion of these lahars leads to a conservative predictive model, for the excluded lahars inundated less area than would a more typical lahar of comparable volume.

Just as we lack historic data for very large lahars, we lack data for small lahars, with $V < 8 \times 10^4$ m^3. Although such small lahars are very common (e.g., Walder and Driedger, 1994), they are seldom thoroughly documented owing to their modest impacts. Therefore, to provide comparative data on small-size events, we include in Table 1 data for nine nonvolcanic debris flows with $V \leq 8 \times 10^4$ m^3. The smallest of these debris flows has $V = 10$ m^3, which matches the volume of experimental debris flows generated at the U.S. Geological Survey debris-flow flume (Iverson, 1997). It is instructive to compare lahar data with the data for these small experimental flows, for

TABLE 1. BASIC DATA RANKED IN ORDER OF FLOW VOLUME

Name of event	Location and date	Data source	Flow volume, V (m^3)	Inundated cross section Area, A (m^2)	Inundated planimetric area, B (m^2)
Osceola	Mount Rainier, United States,. 5000 B.P	Vallance and Scott, 1997	4.0×10^9	1.5×10^5	5.5×10^8
Teteltzingo	Citlaltepetl, Mexico, 18000 B.P.	Carrasco-Núñez et al., 1994	1.8×10^9	N.D.	1.4×10^8
Electron	Mount Rainier, United States, 530–550 B.P	Crandell, 1971	2.5×10^8	3.7×10^4	6×10^7
Round Pass	Mount Rainier, United States, 2700 B.P	Crandell, 1971	2×10^8	N.D.	5×10^7
Dead Man Flat	Mount Rainier, United States, 1100 B.P.	K. Scott et al., 1995; J.W. Vallance, unpublished data	1.8×10^8	1.4×10^4	9.0×10^7
National	Mount Rainier, United States, 500–1800 B.P.	K. Scott et al., 1995; J.W. Vallance, unpublished data	1.5×10^8	1.0×10^4	7.8×10^7
Paradise	Mount Rainier, United States, 4500–5000 B.P.	Crandell, 1971	1×10^8	N.D.	3.4×10^7
Zigzag	Mount Hood, United States, 1700 B.P	J. W. Vallance, unpublished data	7.3×10^7	1.2×10^4	5.5×10^7
Trout Lake	Mount Adams, United States, 6000 B.P.	Vallance, 1998	6.6×10^7	N.D.	2.7×10^7
Middle Fork Nooksack	Mount Baker, United States, 6000 B.P.	Hyde and Crandell, 1978	5×10^7	N.D.	2×10^7
Kautz Creek	Mount Rainier, United States, 1947	Crandell, 1971; Scott and Vallance, 1995	4×10^7	5000	4.5×10^6
Azufrado	Nevado del Ruiz, Columbia, 1985	Fritz et al., 1986; Pierson et al., 1990	4×10^7	2300	3.4×10^7
Molinos Nereidas (Chinchina)	Nevado del Ruiz, Columbia, 1985	Fritz et al., 1986; Pierson et al., 1990	3×10^7	1100	6.0×10^6
Guali	Nevado del Ruiz, Columbia, 1985	Fritz et al., 1986; Pierson et al., 1990	1.6×10^7	2000	1.1×10^7
Salt Creek	Mount Adams, United States, 200 B.P.	Vallance, 1998	1.5×10^7	N.D.	1.6×10^7
Tahoma	Mount Rainier, United States, 400–500 B.P.	Scott et al., 1995	1.5×10^7	1.9×10^4	6.0×10^6
Pine Creek + Muddy River	Mount St. Helens, United States, 1980	Pierson, 1985	1.4×10^7	2100	1.8×10^7
South Fork Toutle	Mount St. Helens, United States, 1980	Janda et al., 1981; Fairchild and Wigmosta, 1983	1.2×10^7	1500	3×10^7
Whitney Creek	Mount Shasta, United States, 1935	Osterkamp et al., 1986	4×10^6	N.D.	8×10^6
Bolum Creek	Mount Shasta, United States, 1897	Osterkamp et al., 1986	1.5×10^6	N.D.	3×10^6
Mabinit Eruption Lahars	Mayon, Philippines, 1984	Rodolfo, 1989	1.2×10^6	200	1.8×10^6
Tahoma Creek	Mount Rainier, United States, 1988	Walder and Driedger, 1994; J.S. Walder, unpublished data	6×10^5	190	1×10^6
Blue Lake	Mount St. Helens, United States, 1980	Major, 1984; Major and Voight, 1986	3.8×10^5	320	7.5×10^5
Butte Canyon	Mount St. Helens, United States, 1980	Major, 1984; Major and Voight, 1986	3.8×10^5	300	5.0×10^5
Mabinit Typhoon Saling	Mayon, Philippines, 1985	Rodolfo, 1989; Rodolfo et al.,1989	3×10^5	200	2×10^5
Middle	Mount St. Helens, United States, 1980	Major, 1984; Major and Voight, 1986	1.4×10^5	N.D.	4.0×10^5
Polallie Creek	Mount Hood, United States, 1980	Gallino and Pierson, 1984; T.C. Pierson, unpublished data	8×10^4	300	4.7×10^5
West Dodson	Columbia Gorge, Oregon, United States, 1996	R. M. Iverson, unpublished data	8×10^4	90	1×10^5
Mayflower Gulch	Tenmile Range, Colorado, United States, 1961	Curry, 1966	1.7×10^4	30	1.6×10^4
Oddstad	Pacifica, California, United States, 1982	Howard et al., 1988	2300	15	N.D.
Big Bend	Pacifica, California, United States, 1982	Howard et al., 1988	660	5	N.D.
Yosemite	Pacifica, California, United States, 1982	Howard et al., 1988	610	11	N.D.
B1	Nigel Pass, Canada, recent	Owens, 1972	300	3.3	2000
N32	Nigel Pass, Canada, recent	Owens, 1972	100	2.7	600
N2	Nigel Pass, Canada, recent	Owens, 1972	10	0.7	200
USGS flume experiments	30 experiments, 1993–1996	Major, 1996; Iverson, 1997	10	$0.4 - 0.6$	200–300

Note: N.D. = no data; USGS = U.S. Geological Survey

TABLE 2. PARAMETERS AND ANALYSIS-OF-VARIANCE STATISTICS
FOR ALTERNATIVE LINEAR MODELS OF LOG-TRANSFORMED LAHAR DATA

Variable	Models for prediction of cross-section area of inundation, A		
	Best-fit regression (Model A1)	Specified 2/3 slope (Model A2)	Specified zero slope (Model A3)
Slope of line	0.6480	0.6667	0
Intercept of line at log $V = 0$	−1.211	−1.301 (=log 0.05)	3.361
Number of data pairs (N)	18	18	18
Residual degrees of freedom (DF)	16	17	17
Residual sum of squares (SS)	1.967	2.008	13.10
Residual mean square (MS)	0.1230	0.1181	0.7708
Standard error of model (σ)	0.351	0.344	0.878
Coefficient of determination (r^2)	0.850	0.847	0
F statistic (comparison to model A1)	N.A.	0.329	90.6

Variable	Models for prediction of planimetric area of inundation, B		
	Best-fit regression (Model B1)	Specified 2/3 slope (Model B2)	Specified zero slope (Model B3)
Slope of line	0.6893	0.6667	0
Intercept of line at log $V = 0$	2.058	2.301 (=log 200)	6.990
Number of data pairs (N)	27	27	27
Residual degrees of freedom (DF)	25	26	26
Residual sum of squares (SS)	1.867	2.064	20.48
Residual mean square (MS)	0.07469	0.07939	0.7879
Standard error of model (σ)	0.273	0.282	0.888
Coefficient of determination (r^2)	0.909	0.900	0
F statistic (comparison to model B1)	N.A.	2.63	249.0

Notes: N.A. = not applicable.

the experimental data are more reproducible and better constrained than are field data. However, because our data for debris flows with $V < 8 \times 10^4$ m³ are not strictly lahar data, we use the debris-flow data only for comparisons and exclude them from statistical analyses.

In Table 1, N.D. represents cases in which no data are available. For most lahars we have data for both the typical cross-sectional area inundated and the total planimetric area inundated in distal valleys (or, as a surrogate, the area covered by deposits), but for other lahars we lack data on cross-section inundation. This poses no problem for statistical analyses because we treat the data for cross-section inundation and planimetric inundation as completely independent sets. We therefore use data from somewhat different groups of lahars to evaluate the hypotheses represented by equations 9 and 10. For lahars in which inundation data from multiple cross sections indicate significant variations with distance downstream, we use data from cross sections nearest the edge of the proximal hazard zone, where maximum cross-section inundation commonly occurs.

Statistical Analyses

Table 2 and Figures 5 and 6 present the results of statistical analyses of the data in Table 1. Figure 5 depicts the data scatter and least-squares best-fit regression line for log A as a function of log V, and Figure 6 depicts the data scatter and least-squares best-fit regression line for log B as a function of log V. Surrounding each regression line are two sets of 95% confidence-interval curves, derived from t- distribution statistics in the standard manner (e.g., Haan, 1977; Weisberg, 1985). The inner (dashed) set of curves encloses the region in which a regression line derived from data with the same parent distribution as the observed data can be expected to fall with a 95% degree of confidence. The size and shape of this confidence interval reflects uncertainty in the mean value of the dependent variable (log A or log B) for any specified value of the independent variable (log V). The outer (dotted) set of confidence-interval curves encloses the region in which knowledge of log V allows future values of the dependent variable (log A or log B) to be predicted with a 95% degree of confidence (cf. Helsel and Hirsch, 1992).

Table 2 lists summary statistics for evaluating hypotheses about the utility of alternative linear models for representing the dependence of log A and log B on log V. Appendix 1 describes the statistical computations. Table 2 is comparable to but somewhat more general than standard analysis of variance (ANOVA) tables used to evaluate simple linear regression models. In our case, we compare each of the two-parameter best-fit linear regression models illustrated in Figures 5 and 6 against two simpler, one-parameter linear models in which the slope is specified and only the intercept (where log $V = 0$) is adjustable.

Comparison of the regression models (A1 and B1 in Table 2) against models with a specified zero slope and an intercept equal to the mean (models A3 and B3 in Table 2) is the standard ANOVA procedure. This procedure tests whether we should reject a null hypothesis which supposes that variation in the independent variable (log V) explains none of the variation in the dependent variable (log A or log B). The F statistic summarizes the comparison, and the very large values of the F statistic listed in Table 2 for the zero-slope models indicate that these models can be rejected with a degree of confidence exceeding 99.5%. In other words, there is strong statistical evidence in favor of regression models with a linear dependence of log A and log B on log V. This is not surprising in light of the obvious correlation illustrated by Figures 5 and 6 and the large values of the coefficient of determination (r^2) listed for the regression models in Table 2.

A different null hypothesis, of particular interest here, supposes that the true dependence of log A and log B on log V can be represented by lines with slopes of 2/3, as specified by equations 9 and 10. We also stipulate that the intercepts of these lines, although adjustable, will be specified to only one significant digit because we believe a more detailed specification implies false precision. A summary of the tests of the "2/3 slope" null hypotheses is provided by the F statistic for models A2 and B2 listed in Table 2. The small values of these F statistics (relative to tabulated values of the F distribution) indicate that we cannot reject the "2/3 slope" null hypotheses with even a 90% degree of confidence. That is, the differences between the best-fit linear regression models (with slopes of 0.6480 and 0.6893) and linear models with specified slopes of 2/3 are slight. This result is not surprising, in light of the similarity of the r^2 statistics for the best-fit regression models and the "2/3 slope" models (Table 2). Nor is the result surprising from a graphical perspective; the lines described by the "2/3 slope" models fall well within the 95% confidence intervals for the regression lines of Figures 5 and 6.

On the basis of the statistical results summarized above, we adopt the

"2/3 slope" predictive models for the cross-sectional and planimetric areas of inundation by lahars:

$$A = 0.05V^{2/3} \qquad (11)$$

$$B = 200V^{2/3}. \qquad (12)$$

There exists the possibility that an unusual event (such as the Tahoma lahar, which plots outside the predictive confidence envelope of Fig. 5) does not behave according to statistical expectations. Nonetheless, even with this limitation, equations 11 and 12 provide useful guidelines for forecasting areas subject to inundation by lahars of various volumes. The utility of equations 11 and 12 is greatest if the equations are used to predict a range of inundation areas for a range of V and to thereby depict a gradation of inundation hazard. Then the statistical uncertainty of equations 11 and 12 (e.g., as measured by standard errors listed in Table 2, which imply roughly a factor of two errors in predicting A or B for a specified V) is superposed on the uncertainty of forecasting V for the next lahar to descend a drainage. Gradational hazard zones reflect both kinds of uncertainty.

IMPLEMENTATION

Figure 7 depicts an algorithmic flow chart that shows how we implement our methodology. Implementation does not require use of GIS, but to automate implementation, we have embedded equation 11 in a GIS that calculates the inundated valley cross-sectional area (A), identifies planimetric areas contributed by successive downstream cross sections, sums the cumulative planimetric areas, and compares the summed planimetric area to the total inundation area (B) defined by equation 12. The suite of programs developed to perform these tasks, LAHARZ (Schilling, 1998), constructs a nested set of inundation-hazard zones in each valley considered, with one zone for each user-specified lahar volume (V). This application of GIS for hazard-zone delineation contrasts with that of Mark and Ellen (1995), who assessed the paths of steepest descent (one grid cell in width) inundated by small debris flows emanating from multiple source areas.

LAHARZ is a suite of Arc/INFO macrolanguage (AML) programs that run within the cell-based Grid program of Arc/INFO (Schilling, 1998). Model input consists of a DEM of topography, derived supplementary grids, specified lahar volumes, and a specified H/L value for the proximal hazard zone boundary (Fig. 7). A preliminary program establishes the position of the proximal hazard zone boundary by computing where the H/L energy cone intersects surface topography. Supplementary Arc/INFO surface hydrology grids (e.g., Jenson and Domingue, 1988) indicate slope directions and the presence of streams. LAHARZ locates a starting cell wherever stream valleys intersect the proximal hazard-zone boundary. Calculations progress downstream cell by cell according to values in the slope-direction grid (Fig. 8A). At each stream cell LAHARZ constructs three valley cross sections, at azimuth intervals of 45° (Fig. 8B).

LAHARZ fills each valley cross section to the appropriate level by first comparing the stream cell elevation to the elevation of adjacent cells along the cross section azimuth (Fig. 8C). The algorithm calculates the difference in elevation between the stream cell and an adjacent cell, multiplies the difference by the cell width (or cell diagonal for diagonal azimuths), and subtracts the result from A as specified by equation 11. After completing this operation for the stream cell, the algorithm then shifts position to outboard adjacent cells and repeats the operation of calculating differences in elevation and subtracting from A the area needed to fill a tier of the cross section. Cross-section filling by subtraction from A continues until A is depleted. In map view, the ends of cross sections determine the lateral limits of inundation.
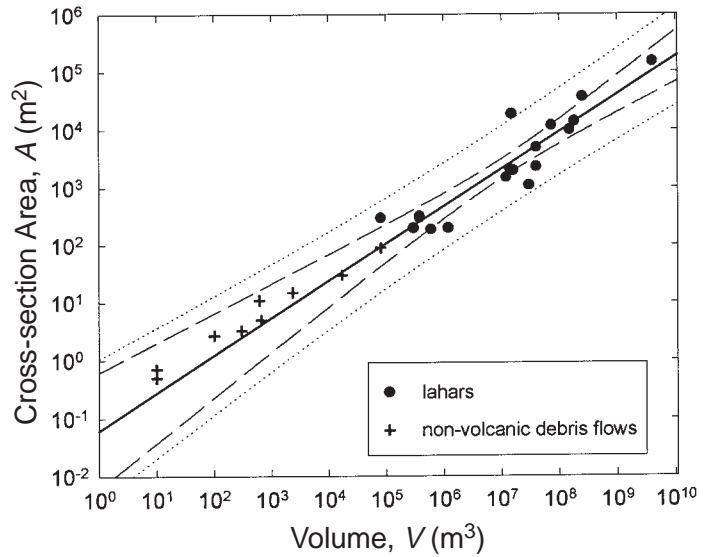

Figure 5. Scatter plot of inundated valley cross-section area A as a function of lahar volume V, constructed using the data of Table 1. The best-fit log-log regression line and 95% confidence intervals for regression (dashed lines) and prediction (dotted lines) are also shown.
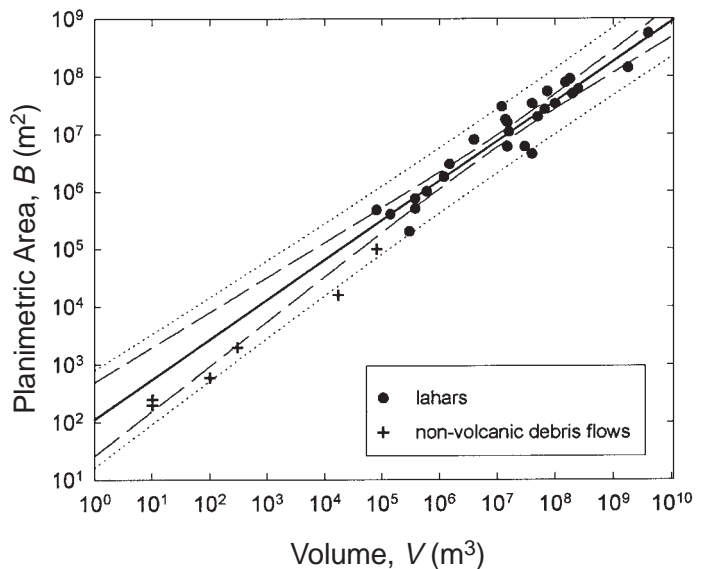

Figure 6. Scatter plot of inundated planimetric area B as a function of lahar volume V, constructed using the data of Table 1. The best-fit log-log regression line and 95% confidence intervals for regression (dashed lines) and prediction (dotted lines) are also shown.

To delineate distal inundation limits, LAHARZ stores the planimetric coordinates of each cell as a cross section is constructed (Fig. 1). Construction of each cross section yields a stored "footprint" of cells (darkly shaded areas in Fig. 8C) that occupies a fraction of the total planimetric area, B (Fig. 1). After LAHARZ calculates a set of three cross sections for a given stream cell, it adds the sections' total footprint to the cumulative inundation footprint from upstream cross sections. Although footprints of a particular cross sec-
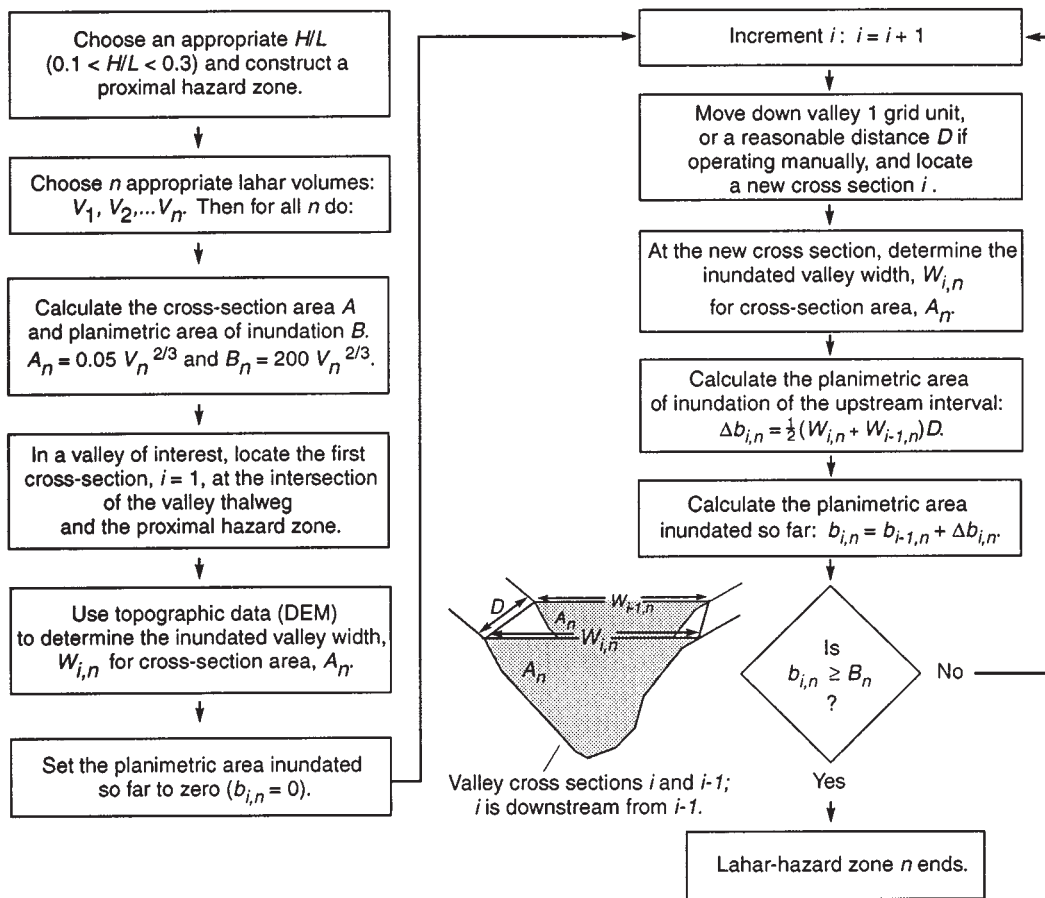
Figure 7. Flow chart of the algorithm used to implement hazard-zone delineation.

tion may overlap with those of other cross sections, individual cells contribute to the cumulative inundation footprint only once. LAHARZ repeatedly compares the cumulative inundation footprint b_n to the total planimetric area B_n specified by equation 12 for each of the user-specified lahar volumes, V_n. When $b_n \geq B_n$, the processing for the specified lahar volume stops, and LAHARZ delineates the distal inundation limit. Calculations for lahars of larger volume continue until either $b_n \geq B_n$ for the larger volume, the program encounters a user-specified stopping cell, or the program encounters the edge of the DEM.

RESULTS

We have applied our methodology to several volcanoes in the northwestern United States, but here we focus on results for Mount Rainier, Washington. Hazards from prospective lahars at Mount Rainier are generally thought to exceed those at any other volcano in the United States. Inundation from past lahars around Mount Rainier has been documented thoroughly, and inundation from future lahars has been predicted on this basis (Crandell, 1971; Scott and Vallance, 1995; K. Scott et al., 1995; Vallance and Scott, 1997). Mount Rainier thus provides an ideal locality for comparing our automated inundation predictions with predictions that use traditional methods.

Figure 9 depicts the computed lahar-inundation hazard map for areas surrounding Mount Rainier, and Figure 10 depicts details of a segment of the map on an expanded scale. To construct the mapped hazard zones, we used five hypothetical lahar volumes, 3.16×10^9, 1×10^9, 3.16×10^8, 1×10^8, and

3.16×10^7 m^3, which correspond to log V = 9.5, 9, 8.5, 8, and 7.5, respectively. The largest of these volumes approximates that of the Osceola mudflow, the largest prehistoric lahar documented at Mount Rainier (Crandell and Waldron, 1956; Dragovich et al., 1994; Vallance and Scott, 1997). The smallest volume approximates that of the largest historic lahar at Mount Rainier, the Kautz Creek lahar of 1947 (Crandell, 1971; K. Scott et al., 1995). Historical records indicate that lahars smaller than 10^7 m^3 are common at Mount Rainier but are unlikely to pose significant hazards outside the proximal hazard zone (Walder and Driedger, 1994; K. Scott et al., 1995).

Despite our use of specific lahar volumes to generate the distal hazard zones in Figures 9 and 10, we rank the hazard in each of the five zones in only relative terms, from "high" to "low." The greatest hazard exists where relatively small, commonplace lahars may cause inundation. The hazard is less in zones likely to be inundated by only the largest, less common lahars. A more quantitative interpretation of the degree of hazard in each zone requires assessment of lahar recurrence probabilities—an assessment complicated by factors we describe in the following Discussion section.

We delineated the proximal hazard zone boundary in Figures 9 and 10 by the intersection of the topographic surface with an energy cone specified by $H/L = 0.23$. This value approximates the value $H/L = 0.235$ used by Hoblitt et al. (1995) in an assessment of hazards at Mount Rainier. Different choices of H/L for the proximal hazard zone would shift the upstream and downstream limits of the computed distal hazard zones, but would not affect the lateral limits of these zones. In this regard, our methodology is robust with respect to uncertainty about the extent of the proximal hazard zone.

Figure 10 illustrates details of computed lahar hazard zones for a reach of

the Puyallup River valley on the western flank of Mount Rainier and compares them with a hazard zone constructed by K. Scott et al. (1995) on the basis of deposits left by the 2.5×10^8 m³ Electron mudflow about 500 yr ago. Similar comparisons in other valleys yield similar results. The large scale of Figure 10 reveals the rectilinear boundaries of the computational grid cells, which reflect the resolution (62.5 m) of the base DEM. For a lahar so small or so depleted in volume or discharge that 62.5 m is a significant fraction of the inundated valley width, a DEM of greater resolution is required to obtain meaningful results. However, lahars with volumes greater than 3×10^7 m³, like those used to generate Figures 9 and 10, generally inundate broad (>62.5 m) swaths of valleys or fill valleys wall to wall. In these instances the 62.5 m DEM resolution appears adequate for all except the most depleted, distal stages of runout.

DISCUSSION

We discuss three issues that arise in applying our methodology and interpreting the results. (1) How severe are limitations that result from automated mapping of hazard-zone boundaries and use of DEMs for defining base topography? (2) Can mapped gradations in lahar-inundation hazard provide a basis for probabilistic hazard assessment? (3) Do significant distinctions exist between inundation patterns produced by lahars and those produced by rock avalanches and nonvolcanic debris flows?

Limitations of Automated Mapping and DEMs

Our automated mapping methodology has limitations due to the limited resolution and accuracy of the base DEMs. Some limitations, such as inability to assess waning stages of lahar runout confined within stream channels, are relatively obvious. Other limitations are less immediately apparent. One limitation involves the construction of a finite number of prospective inundation cross sections due to the finite number of DEM grid cells and finite number of cross-section azimuths we consider. This procedure creates hazard-zone boundaries that may in places appear irregular or "ragged" when viewed in detail (e.g., Figs. 9 and 10). Judicious smoothing of these ragged edges may in places be warranted before hazard maps are produced in final form—although we have performed no smoothing of the maps we present here. Another limitation involves neglect of the possible influence of cultural features (e.g., reservoirs) on the behavior of lahars. Our method treats all topographic features the same, regardless of whether cultural features are present. A related limitation involves sensitivity of our method to subtle variations of digital topography in areas of low relief. This sensitivity can pose a problem if the base DEM contains information that does not faithfully represent the true shape of landforms. For example, an elevated railroad grade or levee on an otherwise nearly planar flood plain will influence predicted lahar inundation only if the base DEM contains data that depict the elevated feature. On the other hand, a narrow gap in a ridgeline might permit a real lahar to issue through the ridge and to inundate a considerable area on the other side. If this gap is not represented in the base DEM, our methodology will ignore its presence and potential influence. For this reason, computed hazard zones should be viewed as guidelines for interpretation and not as ironclad predictions.

Our methodology does not account for the tendency of lahars to run up against the outside bank of channel bends or for accrual of hazard where two or more valleys coalesce downstream (e.g., Fig. 9). If compelling data become available, a runup algorithm can be added to cross-section inundation calculations. More information on lahar probabilities would be necessary to compute the cumulative hazard where multiple hazard zones coalesce downstream.
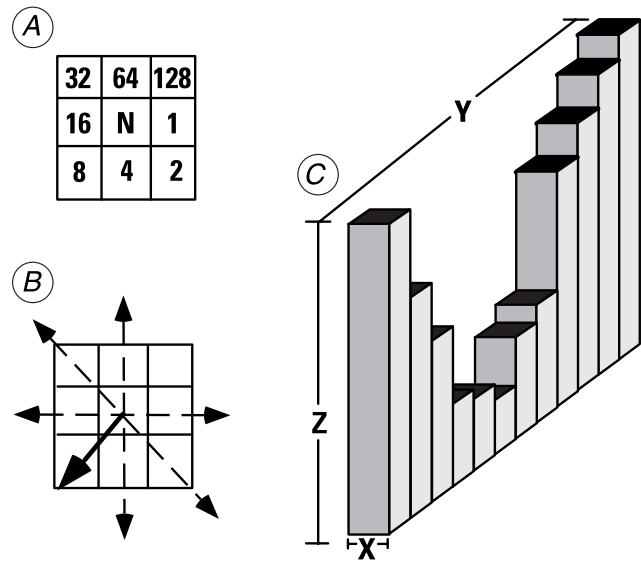

Figure 8. Schematics illustrating geographic information system concepts used to construct cross sections. (A) Cell N holds one of the values of the surrounding cells, each of which indicates a computed direction for flow out of cell N. For example, if N = 4, the direction of flow out of cell N is south. (B) The solid arrow designates a computed flow direction, and the dashed arrows designate directions of the three computed cross sections. (C) Column heights designate the elevations along a valley cross section as represented in a hypothetical DEM. The lowest column designates the stream cell. After LAHARZ fills the vertical cross-section area, A, it stores the darkly shaded areas (i.e., the surface areas of the cells) and deducts this "footprint" from the total planimetric area, B.

Probabilistic Hazard Assessment

Although we rank the inundation hazard portrayed in Figures 9 and 10 only in qualitative terms, from high to low, a more quantitative, probabilistic interpretation is clearly desirable. In principle, probable recurrence intervals can be assigned to lahars of differing volumes in any valley downstream from a volcano, and this information can be used to interpret quantitatively maps such as those in Figures 9 and 10. Lahar volume (rather than peak discharge) is the most logical measure of event magnitude for assessing lahar recurrence probabilities, not only because volume is the basis on which we assess inundation areas, but also because lahars are episodic phenomena that have unambiguous source areas and tangible end points in space and time. In this respect lahars are more like landslides and earthquakes than rainfall-runoff floods.

As a working hypothesis we might assume that recurrence intervals for lahars increase roughly in proportion to event magnitude raised to some power, analogous to Gutenberg-Richter recurrence intervals for earthquakes (e.g., Rundle, 1989). For example, on the basis of limited data for Mount Rainier summarized by Crandell (1971) and K. Scott et al. (1995), we speculate that lahar recurrence at Mount Rainier might obey a relationship like that shown in Figure 11. If Figure 11 were accurate, it would provide all information necessary to interpret Figures 9 and 10 as probabilistic hazards maps. However, such a naive interpretation ignores variation from valley to valley of inundation probabilities within specific hazard zones, and it ignores dependence of that variation on deterministic factors such as slope angle and hydrothermal alteration (cf. Crowley and Zimbleman, 1997). These
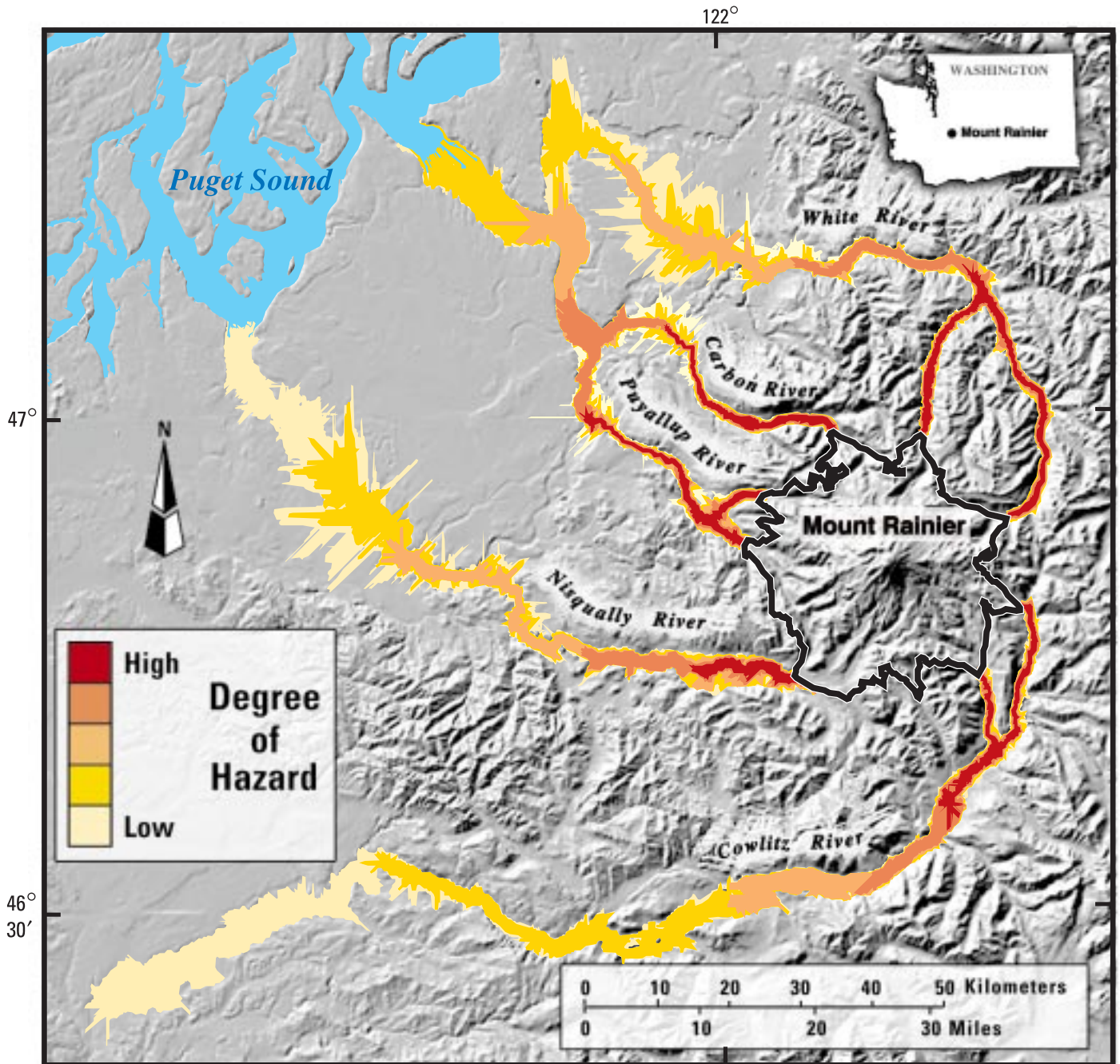
Figure 9. Lahar-inundation hazard map constructed by applying LAHARZ to the Mount Rainier region in western Washington. Topography is depicted by shaded relief. The proximal hazard zone enclosed by the dark line surrounding Mount Rainier is subject to diverse hazards, including lahars.

complications demonstrate that recurrence relationships like that shown in Figure 11 require critical evaluation and refinement prior to practical application. Until such work is completed we can nonetheless portray a gradation of hazards on the basis of projected inundation from a spectrum lahars of increasing size and decreasing (but as yet unspecified) probability.

Lahars, Rock Avalanches, and Nonvolcanic Debris Flows

Many catastrophic lahars evolve from rock avalanches, but not all rock avalanches spawn lahars (cf. Iverson et al., 1997). To draw distinctions between the two processes, it is useful to compare the results of our statistical
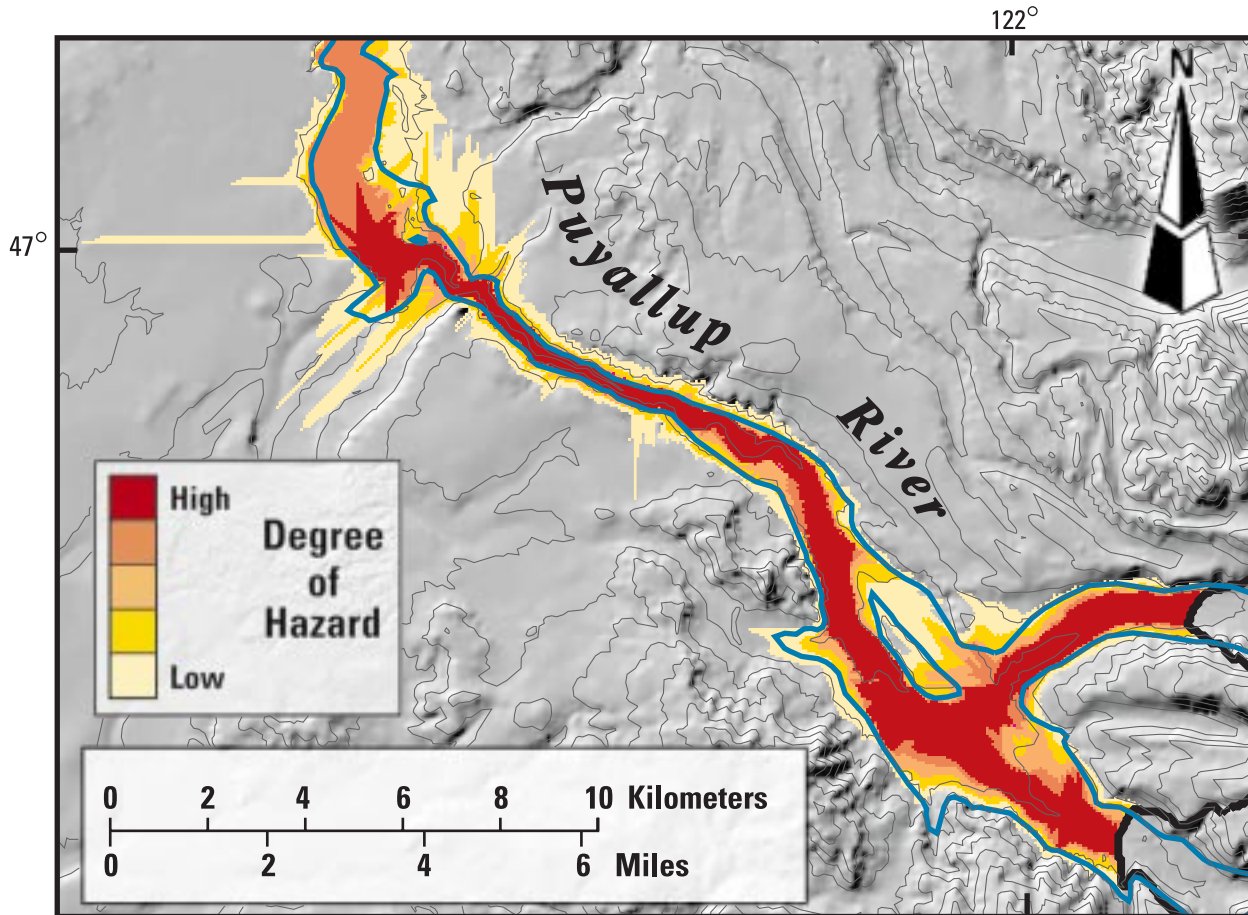
Figure 10. Enlarged segment of the lahar-inundation hazard map (Fig. 9) for a reach of the Puyallup River valley west of Mount Rainier. Topography is depicted by 100 m contours in addition to shaded relief. Dark blue lines that parallel the Puyallup River are the lahar inundation hazard-zone boundaries established by K. Scott et al. (1995) on the basis of deposits of the Electron mudflow.

and scaling analyses of lahars with analogous results for rock avalanches. Li (1983) used log-log axes like those of our Figure 6 to plot planimetric areas inundated by rock avalanches as a function of avalanche volume, and Hungr (1990) interpreted Li's data in the context of geometric analyses of avalanche deposits. Li (1983) found that the best-fit regression line for 70 rock avalanches ranging from 10^5 to 10^{10} m^3 in volume was (using our notation) $B = 80V^{0.5667}$, with $r^2 = 0.78$. Hungr (1990) noted that the exponent 0.5667 in Li's (1983) equation differed little from the value 2/3 expected if geometric similarity of deposits prevailed, and he demonstrated graphically that a line described approximately by $B = 10V^{2/3}$ fits Li's (1983) data reasonably well. The similarity of the rock avalanche equation ($B = 10V^{2/3}$) to our equation 12 implies that rock avalanches obey scaling rules similar to those for lahars. However, the difference in proportionality coefficients in the avalanche and lahar equations (10 vs. 200) implies that lahars typically inundate areas 20 times larger than do rock avalanches of similar size. This result is not surprising because the mobility of lahars is enhanced by strong solid-fluid interactions that are absent in rock avalanches (Iverson, 1997).

To place the distinction between rock avalanches and lahars in more concrete terms, consider an avalanche and lahar that each have a volume of 10^9 m^3 (1 km^3). On the basis of the equations discussed herein, the avalanche can be expected to inundate an area of 10^7 m^2, creating a deposit that aver-

ages 100 m in thickness. In contrast, the lahar can be expected to inundate an area of 2×10^8 m^2, creating a deposit that averages 5 m in thickness. The difference in calculated inundation areas also implies that lahars are apt to travel much further downstream than are rock avalanches of comparable volume, although the distance traveled depends strongly on the degree of flow-path confinement by valley walls or other topographic features. If the planimetric shapes of lahar paths and avalanche paths were identical, the equations discussed herein would indicate that lahars on average travel about $\sqrt{20}$ (~4.5) times farther than avalanches of similar volume. Instead, limited data indicate that lahars commonly travel about twice as far as avalanches of comparable volume (Iverson, 1997), which indicates that lahars commonly undergo more lateral spreading than avalanches. Greater lateral spreading appears to result from lahars' greater tendency to travel into lowland areas where valleys widen and topography exerts fewer constraints (e.g., Fig. 9).

Data for small, nonvolcanic debris flows provide another opportunity for comparing the inundation patterns of lahars with those of related phenomena. Debris flows exhibit a variety of compositions and behaviors intermediate between those of wet rock avalanches and sediment-laden water floods (Iverson, 1997), but small debris flows commonly contain greater concentrations of large clasts than do large lahars (cf. Crandell, 1971;
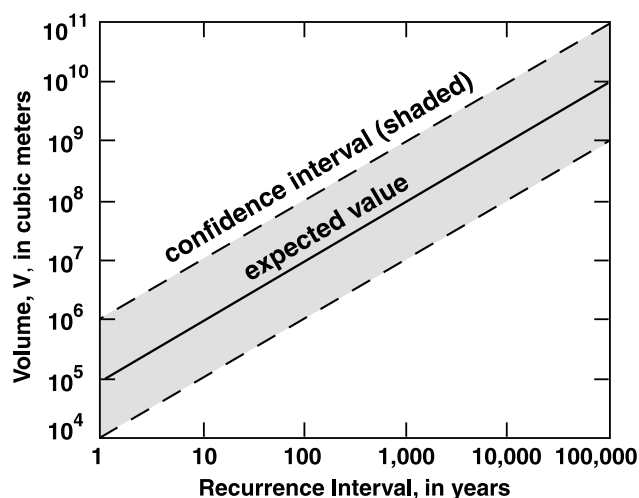
Figure 11. Hypothetical relationship between lahar volume and lahar recurrence at Mount Rainier. Such relationships necessarily involve some uncertainty (depicted by the confidence interval on the diagram) for data sets that are finite.

Takahashi, 1991). The data for nonvolcanic debris flows plotted in Figures 5 and 6 depart systematically from the trends of the lahar data. The departures indicate that small, nonvolcanic debris flows inundate channel cross sections that are larger, but planimetric areas that are smaller, than would be anticipated from the lahar data. The nonvolcanic debris flows appear on average to move less fluidly and form proportionately thicker deposits than do most lahars. This difference in inundation patterns could represent a scale effect, or it could indicate that the nonvolcanic debris flows are less mobile than lahars. Perhaps owing to their concentrations of large clasts, small, nonvolcanic debris flows maintain higher frictional resistance and occupy a niche somewhat closer to rock avalanches in the spectrum of compositions and behaviors that are feasible for gravity-driven sediment-water mixtures (Iverson, 1997).

CONCLUSIONS

Our analytical, statistical, and computational results support the following conclusions.

1. The semiempirical equations $A = 0.05V^{2/3}$ and $B = 200V^{2/3}$ provide an objective, reproducible means of predicting valley cross-sectional areas (A) and planimetric areas (B) inundated by lahars of various volumes (V). Lahar-inundation hazard zones constructed using these equations mimic hazard zones delineated on the basis of detailed field investigations. Statistical uncertainties associated with the mathematical predictions reflect the range of behavior exhibited by diverse lahars.

2. Delineation of hazard zones using the equations $A = 0.05V^{2/3}$ and $B = 200V^{2/3}$ can be accomplished manually, but is expedited by use of digital elevation models and GIS. The suite of GIS programs LAHARZ provides a rapid, automated means of applying our predictive equations to regions around volcanoes.

3. Hazards from prospective lahars can be inferred to decrease as distances from volcanoes and elevations above valley floors increase. Hazard maps constructed using LAHARZ portray this gradation in hazard by depicting nested hazard zones for lahars of various volumes. This qualitative gradation in hazard can be quantified if data are available to compute expected recurrence intervals of lahars of various volumes.

4. On average, lahars of any volume inundate planimetric areas roughly 20 times larger than those inundated by rock avalanches of similar volume. This fundamental difference in the behavior of rock avalanches and lahars indicates that distinctions between these processes may be important in hazard assessments.

ACKNOWLEDGMENTS

APPENDIX. STATISTICAL METHODS

Following Weisberg (1985), all quantities listed in Table 2 are derived from two fundamental quantities that characterize each model: the residual degrees of freedom (DF) and residual sum of squares (SS). For each model, $DF = N - P$, where N is the number of observations (lahars) in the data set, and P is the number of fitted model parameters ($P = 2$ for regression models, and $P = 1$ for the models with specified slopes). For each model,

$$SS = \sum_{i=1}^{N}\left(y_i - y_{pred}\right)^2, \tag{A1}$$

where y_i is a value of the dependent variable (log A or log B), and y_{pred} is the associated value of this variable predicted by the linear model y_{pred} = intercept + (slope × log V). In the regression model two free parameters (slope and intercept) are calibrated mathematically by minimizing SS. In the other (null-hypothesis) models, the slope is specified as either 0 or 2/3, and only the intercept is calibrated. For the zero-slope model the intercept equals the mean value of the dependent variable (log A or log B). For all models the residual mean square is defined by $MS = SS \div DF$, and the standard error is $\sigma = \sqrt{MS}$.

The statistics r[2] and F listed in Table 2 provide quantitative comparisons between alternative linear models. The coefficient of determination (r[2]) compares the goodness of fit of models having nonzero slopes (A1, A2, B1, and B2 in Table 2) to the goodness of fit of a zero-slope model of the same data. We compute the coefficient from the formula

$$r^2 = 1 - \frac{SS_{\text{nonzero slope}}}{SS_{\text{zero slope}}}, \tag{A2}$$

which reduces to the standard form given in most statistics books if $SS_{\text{nonzero slope}}$ refers to the regression model. The extent to which r[2] exceeds 0 and approaches 1 indicates the extent to which a model with nonzero slope surpasses the zero-slope model in describing the data trend.

The F statistic compares the goodness of fit of models having differing residual degrees of freedom. We compare the zero-slope and 2/3-slope "null" models, with $N - 1$ residual degrees of freedom, to the regression models with $N - 2$ residual degrees of freedom. We compute F from the formula

$$F = \frac{\left(SS_{\text{null}} - SS_{\text{regression}}\right)\big/\left(DF_{\text{null}} - DF_{\text{regression}}\right)}{SS_{\text{regression}}\big/DF_{\text{regression}}}. \tag{A3}$$

Interpretation of the computed value of F requires comparison to values of the F distribution, tabulated in most statistics books (e.g., Haan, 1977). A match between the computed and tabulated values of F establishes the probability (α) of erroneously rejecting the null hypothesis when the null hypothesis is actually correct. Computed values of F that are larger than tabulated values provide evidence for rejecting the null hypothesis at the $1 - \alpha$ confidence level. On the other hand, computed values of F that are smaller than tabulated values indicate that the null hypothesis cannot be rejected at the $1 - \alpha$ confidence level.

REFERENCES CITED

Carrasco-Núñez, G., Vallance, J. W., and Rose, W. I., 1994, A voluminous avalanche-induced lahar from Citlaltepetl volcano, Mexico: Implications for hazard assessment: Journal of Volcanology and Geothermal Research, v. 59, p. 35–46.

Costa, J. E., 1997, Hydraulic modeling for lahar hazards at Cascades Volcanoes: Environmental and Engineering Geoscience, v. 3, p. 21–30.

Crandell, D. R., 1971, Postglacial lahars from Mount Rainier volcano, Washington: U.S. Geological Survey Professional Paper 677, 73 p.

Crandell, D. R., and Mullineaux, D. R., 1967, Volcanic hazards at Mount Rainier: U.S. Geological Survey Bulletin 1238, 26 p.

Crandell, D. R., and Mullineaux, D. R., 1975, Technique and rationale of volcanic-hazards appraisals in the Cascade Range, northwestern United States: Environmental Geology, v. 1, p. 23–32.

Crandell, D. R., and Waldron, H. H., 1956, A recent volcanic mudflow of exceptional dimensions from Mount Rainier, Washington: American Journal of Science, v. 254, p. 349–362.

Crowley, J. K., and Zimbleman, D. R., 1997, Mapping hydrothermally altered rocks on Mount Rainier, Washington, with airborne visible/infrared imaging spectrometer (AVIRIS) data: Geology, v. 25, p. 559–562.

Curry, R. R., 1966, Observation of alpine mudflows in the Tenmile Range, Colorado: Geological Society of America Bulletin, v. 77, p. 771–776.

Dragovich, J. D., Pringle, P. T., and Walsh, T. J., 1994, Extent and geometry of the mid-Holocene Osceola Mudflow in the Puget Lowland—Implications for Holocene sedimentation and paleogeography: Washington Geology, v. 22, p. 3–26.

Fairchild, L. H., 1987, The importance of lahar initiation processes, *in* Costa, J. E., and Wieczorek, G. F., eds., Debris flows/avalanches: Process, recognition, and mitigation: Geological Society of America Reviews in Engineering Geology, v. 7, p. 51–61.

Fairchild, L. H., and Wigmosta, M., 1983, Dynamic and volumetric characteristics of the 18 May 1980 lahars on the Toutle River, Washington: Proceedings of the Symposium on Erosion Control in Volcanic Regions: Japan Public Works Research Institute Technical Memorandum 1908, p. 131–154.

Fritz, W. J., Sigurdsson, H., and Naranjo, J. L., 1986, Volume, distribution and generation of lahars from the 13 November 1985 eruption of Nevado del Ruiz, Columbia [abs.]: Eos (Transactions, American Geophysical Union), v. 67, p. 406.

Gallino, G. L., and Pierson, T. C., 1984, The 1980 Polallie Creek debris flow and subsequent dambreak flood, East Fork Hood River basin, Oregon: U.S. Geological Survey Open-File Report 84-578, 37 p.

Haan, C. T., 1977, Statistical methods in hydrology: Ames, Iowa State University Press, 378 p.

Hayashi, J. N., and Self, S., 1992, A comparison of pyroclastic flow and debris avalanche mobility: Journal of Geophysical Research, v. 97, p. 9063–9071.

Helsel, D. R., and Hirsch, R. M., 1992, Statistical methods in water resources: Amsterdam, Elsevier, 529 p.

Henderson, F. M., 1966, Open channel flow: New York, Macmillan, 522 p.

Hoblitt, R. P., Walder, J. S., Driedger, C. L., Scott, K. M., Pringle, P. T., and Vallance, J. W., 1995, Volcano hazards from Mount Rainier, Washington: U.S. Geological Survey Open-File Report 95-273, 10 p.

Howard, T. R., Baldwin, J. E., and Donley, H. F., 1988, Landslides in Pacifica, California, caused by the storm, *in* Landslides, floods and marine effects of the storm of January 3–5, 1982, in the San Francisco Bay Region, California: U.S. Geological Survey Professional Paper 1434, p. 163–183.

Hungr, O., 1990, Mobility of rock avalanches: Report of the National Research Institute for Earth Science and Disaster Prevention, Japan, v. 46, p. 11–20.

Hyde, J. H., and Crandell, D. R., 1978, Postglacial volcanic deposits at Mount Baker, Washington, and potential hazards from future eruptions: U.S. Geological Survey Professional Paper 1022-C, 17 p.

Iverson, R. M., 1997, The physics of debris flows: Reviews of Geophysics, v. 35, p. 245–296.

Iverson, R. M., Reid, M. E., and LaHusen, R. G., 1997, Debris-flow mobilization from landslides: Annual Review of Earth and Planetary Sciences, v. 25, p. 85–138.

Janda, R. J., Scott, K. M., Nolan, K. M., and Martinson, H. A., 1981, Lahar movement, effects and deposits, in the 1980 Eruptions of Mount St. Helens, Washington: U.S. Geological Survey Professional Paper 1250, p. 461–478.

Jenson, S. K., and Domingue, J. O., 1988, Extracting topographic structure from digital elevation data for geographic information system analysis: Photogrammetric Engineering and Remote Sensing, v. 54, p. 1593–1600.

Laenen, A., and Hansen, R. P., 1988, Simulation of three lahars in the Mount St. Helens area, Washington, using a one-dimensional unsteady-state streamflow model: U.S. Geological Survey Water-Resources Investigations Report 88-4004, 20 p.

Li Tianchi, 1983, A mathematical model for predicting the extent of a major rockfall: Zeitschrift für Geomorphologie, v. 27, p. 473–482.

Macedonio, G., and Pareschi, M. T., 1992, Numerical simulation of some lahars from Mount St. Helens: Journal of Volcanology and Geothermal Research, v. 54, p. 65–80.

Major, J. J., 1984, Geologic and rheologic characteristics of the May 18, 1980 southwest flank lahars at Mount St. Helens, Washington [Master's thesis]: University Park, Pennsylvania State University, 225 p.

Major, J. J., 1996, Experimental studies of deposition by debris flows: Process, characteristics of deposits, and effects of pore-fluid pressure [Ph.D. dissert.]: Seattle, University of Washington, 341 p.

Major, J. J., and Voight, B., 1986, Sedimentology and clast orientations of the 18 May 1980 southwest-flank lahars, Mount St. Helens, Washington: Journal of Sedimentary Petrology, v. 56, p. 691–705.

Malin, M. C., and Sheridan, M. F., 1982, Computer-assisted mapping of pyroclastic surges: Science, v. 217, p. 637–640.

Mark, R. K., and Ellen, S. D., 1995, Statistical and simulation models for mapping debris-flow hazard, *in* Carrara, A., and Guzzetti, F., eds., Geographical information systems in assessing natural hazards: Amsterdam, Kluwer Academic, p. 93–106.

Osterkamp, W. R., Hupp, C. R., and Blodgett, J. C., 1986, Magnitude and frequency of debris flows, and areas of hazard on Mount Shasta, northern California: U.S. Geological Survey Professional Paper 1396-C, 21 p.

Owens, I. F., 1972, Morphological characteristics of alpine mudflows in the Nigel Pass area, *in* Slaymaker, O., and McPherson, H. J., eds., Mountain geomorphology: Vancouver, Tantalus Research, p. 93–100.

Pierson, T. C., 1985, Initiation and flow behavior of the 1980 Pine Creek and Muddy River lahars, Mount St. Helens, Washington: Geological Society of America Bulletin, v. 96, p. 1056–1069.

Pierson, T. C., 1995, Flow characteristics of large eruption-triggered debris flows at snow-clad volcanoes: Constraints for debris-flow models: Journal of Volcanology and Geothermal Research, v. 66, p. 283–294.

Pierson, T. C., and Scott, K. M., 1985, Downstream dilution of a lahar: Transition from debris flow to hyperconcentrated streamflow: Water Resources Research, v. 21, p. 1511–1524.

Pierson, T. C., Janda, R. J., Thouret, J. C., and Borerro, C. A., 1990, Perturbation and melting of snow and ice by the 13 November 1985 eruption of Nevado del Ruiz, Colombia, and consequent mobilization, flow, and deposition of lahars: Journal of Volcanology and Geothermal Research, v. 41, p. 17–66.

Rodolfo, K. S., 1989, Origin and early evolution of lahar channel at Mabinit, Mayon Volcano, Philippines: Geological Society of America Bulletin, v. 101, p. 414–426.

Rodolfo, K. S., Arguden, A. T., Solidum, R. U., and Umbal, J. V., 1989, Anatomy and behavior of a posteruptive rain lahar triggered by a typhoon on Mayon Volcano, Philippines: Bulletin of the International Association of Engineering Geology, v. 40, p. 55–66.

Rundle, J. B., 1989, Derivation of the complete Gutenberg-Richter magnitude-frequency relation using the principle of scale invariance: Journal of Geophysical Research, v. 94, p. 12337–12342.

Savage, S. B., and Hutter, K., 1989, The motion of a finite mass of granular material down a rough incline: Journal of Fluid Mechanics, v. 199, p. 177–215.

Schilling, S. P., 1998, LAHARZ: GIS programs for automated delineation of lahar hazard zones, U.S. Geological Survey Open-file Report.

Scott, K. M., and Vallance, J. W., 1995, Debris flow, debris avalanche, and flood hazards at and downstream from Mount Rainier, Washington: U.S. Geological Survey Hydrologic Investigations Atlas HA-729, 9 p.

Scott, K. M., Vallance, J. W., and Pringle, P. T., 1995, Sedimentology, behavior, and hazards of debris flows at Mount Rainier, Washington: U.S. Geological Survey Professional Paper 1547, 56 p.

Scott, W. E., Iverson, R. M., Vallance, J. W., and Hildreth, W., 1995, Volcano hazards in the Mount Adams region, Washington: U.S. Geological Survey Open-File Report 95-492, 11 p.

Siebert, L., 1984, Large volcanic debris avalanches: Characteristics of source areas, deposits, and associated eruptions: Journal of Volcanology and Geothermal Research, v. 22, p. 163–197.

Takahashi, T., 1991, Debris flow: Rotterdam, Netherlands, Balkema, 165 p.

Vallance, J. W., 1998, Postglacial lahars and potential volcanic hazards in the White Salmon River drainage, Mount Adams, Washington: U.S. Geological Survey Bulletin 2161.

Vallance, J. W., and Scott, K. M., 1997, The Osceola mudflow from Mount Rainier: Sedimentology and hazards implications of a huge clay-rich debris flow: Geological Society of America Bulletin, v. 109, p. 143–163.

Vignaux, M., and Weir, G., 1990, A general model of Mt. Ruapehu lahars: Bulletin of Volcanology, v. 52, p. 381–390.

Walder, J. S., and Driedger, C. L., 1994, Rapid geomorphic change caused by glacial outburst floods and debris flows along Tahoma Creek, Mount Rainier, Washington, USA: Arctic and Alpine Research, v. 26, p. 319–327.

Weisberg, S., 1985, Applied linear regression (second edition): New York, Wiley, 324 p.